Distinct Spatial and Functional Dynamics for Alpha and Gamma Oscillations in Human Visual Cortex

by

Sanaz Ghaffari SarvarMaleki

A thesis submitted to the
Department of Computer Science
in conformity with the requirements for
the degree of Master of Science

Bishop's University
Canada
January 2026

Abstract

Visual processing in the human brain relies on the functional organization of the visual cortex, characterized by retinotopic mapping and orientation tuning. Retinotopic mapping preserves the spatial layout of the visual field within cortical regions such as V1, V2, and V3, while orientation tuning enables neurons to respond selectively to specific stimulus angles, supporting edge detection and shape perception. Neural oscillations, particularly in the alpha (8–12 Hz) and gamma (30–80 Hz) frequency bands, play a central role in regulating these processes. Alpha rhythms are associated with inhibitory control, gating irrelevant information and facilitating selective attention, whereas gamma rhythms promote coherent communication between cortical areas, integrating sensory information for precise spatial and feature-specific processing. Electroencephalography (EEG) offers a high-temporal-resolution method for investigating these dynamics, revealing how alpha suppression and gamma enhancement are modulated by visual stimuli. Experimental designs employing retinotopic and orientation-specific stimuli—such as rotating wedges, expanding rings, and oriented gratings—have shown that gamma responses are strongly spatially tuned and linearly summate across visual subfields, while alpha responses are broader, less spatially specific, and can occur even without direct visual input. Furthermore, gamma activity exhibits robust orientation selectivity, with oblique gratings often evoking stronger responses than horizontal or vertical ones, whereas alpha modulation is comparatively weaker and more variable. These findings indicate distinct but interacting circuit mechanisms underlying alpha and gamma rhythms, reflecting differences in spatial specificity, feature tuning, and their roles in visual attention. Understanding these relationships provides a mechanistic framework for linking large-scale neural dynamics to perception, with implications for both basic neuroscience and applications such as brain–computer interfaces and clinical interventions targeting visual and attentional disorders.

Acknowledgments

First and foremost, I thank my professor, Dr. Russell Butler, for his unwavering support, insightful guidance, and invaluable mentorship. I am grateful to the Computer Science Department faculty and my defense committee for their thoughtful counsel, and to the Bishop's Graduate Entrance Scholarship Foundation for generous funding that made this work possible. To my mother, whose love and sacrifices sustain me, and to my sister, Sorayya, whose steadfast encouragement has been a constant strength—thank you. I also honor my late father, whose wisdom and love continue to guide me. This work is dedicated to all who supported and believed in me.

Contents

List of Figures

Chapter 1

Introduction

Gamma (40–80 Hz) and alpha (8–12 Hz) oscillations are prominent visual cortex rhythms with opposing functional associations. Alpha, first described by Berger in 1929 [3] and later characterized by Adrian and Matthews [1], is high during eyes-closed rest and suppresses upon visual stimulation ("blocking"), reflecting an idling or inhibitory state. Gamma, discovered later in animal visual cortex [17], emerges during active visual processing, reflecting synchronous excitatory–inhibitory interactions. Human EEG (Electroencephalography), MEG (Magnetoencephalography), and ECoG (Electrocorticography) studies confirm that stimulus-induced gamma is linked to feature encoding, perceptual binding, and attention [48]. At the same time, gamma is highly stimulus-dependent, robust to high-contrast gratings but often weak to natural images, even when broadband activity is strong, indicating that narrowband gamma is not necessary for all forms of seeing [21]. Methodological advances now allow more reliable detection and localization of these rhythms, including on-scalp OPM-MEG (Optically Pumped Magnetometer Magnetoencephalography) that boosts visual gamma SNR (Signal-to-Noise Ratio) relative to conventional SQUID (Superconducting Quantum Interference Device) arrays [25]. Thus, gamma generally marks active processing, whereas alpha marks relative inactivity or inhibition [10], with important boundary conditions set by stimulus class and measurement sensitivity [21, 25].

Their tuning and spatial profiles differ sharply. Gamma is localized, retinotopically specific, and sharply tuned to features such as orientation, spatial frequency, and motion direction, sometimes mirroring local spiking preferences [11, 14, 51]. Sustained induced gamma carries a stimulus-specific temporal-frequency "fingerprint" that varies with spatial frequency [18], and its magnitude scales with stimulus size, saturating at larger fields [39]. Gamma peak frequency increases for moving vs. static patterns [47] and tracks motion velocity [38], consistent with sensitivity to input drive. Beyond achromatic patterns, gamma shows feature selectivity to orientation and color [32] and depends on hue/input strength [46]. At the macroscale, gamma peak frequency covaries with early visual cortex surface

area [44], though this structure–gamma link is not always replicated for amplitude or frequency [39], underscoring inter-individual variability. Alpha shows weak feature tuning: most salient visual stimuli suppress alpha regardless of specific features, with only modest orientation dependence [10]. Critically, a large body of EEG work demonstrates retinotopic, anticipatory alpha synchronization over cortex representing to-be-ignored space, consistent with active inhibitory gating [30, 41, 56], and lateralized alpha immediately before target onset predicts detection benefits at the attended location [50]. In sum, gamma reflects local, feature-selective excitation, whereas alpha reflects diffuse inhibitory control, generally inversely related to visual drive.

Gamma and alpha oscillations appear to mediate complementary roles in cortical communication. Converging evidence links gamma to feedforward sensory signaling and alpha to feedback modulation and inhibition [14, 35]. Human MEG with directed-influence analyses shows that feedforward interactions peak in the gamma band, whereas feedback interactions peak in alpha–beta, aligning a frequency-resolved functional hierarchy with macaque anatomical hierarchy [35]. Complementarily, simultaneous EEG–laminar fMRI (Functional Magnetic Resonance Imaging) reveals layer-specific coupling: gamma power correlates positively with superficial-layer BOLD, whereas alpha (and beta) correlate negatively with deeper and superficial layers, consistent with feedback-related inhibition [43]. Together, these results strengthen the view that gamma predominates in feedforward drive while alpha–beta implement top-down control.

Although the feedforward–feedback framework provides a useful starting point, important gaps remain in understanding how gamma and alpha relate in the human visual cortex. It is still unclear whether they emerge from a single push–pull circuit or from largely independent neural generators, perhaps in different cortical layers or cell populations. The new laminar and causality evidence [35, 43] suggests partly segregated generators, yet electrophysiology shows stimulus classes where narrowband gamma can be minimal despite strong processing [21], arguing against a simple obligatory antagonism. Likewise, the determinants of gamma frequency (motion, velocity, orientation, color, cortical anatomy) versus amplitude (size, contrast, field coverage) can dissociate [32, 38, 39, 44, 46, 47], leaving open whether alpha–gamma "push–pull" holds uniformly across contexts or breaks under specific feature/spatial regimes.

One underexplored dimension concerns how spatial integration shapes these rhythms. In primate V1, large visual stimuli can synchronize local gamma into a coherent "global gamma" spanning millimeters of cortex [14, 36, 51]. Human MEG shows that gamma amplitude grows with stimulus size and can become subadditive for composite fields [39], and that full-field/annular stimulation maximizes gamma at the expense of localization precision [37]. Gamma frequency rises for moving patterns and scales with velocity [38, 47], and color/input strength further

modulates gamma [46]. What remains unclear is whether this integration is accompanied by proportionally broader alpha suppression, or whether alpha reflects more context-dependent attentional gating whose spatial footprint depends on task demands, despite robust evidence for retinotopic alpha inhibition [30, 41, 50, 56]. Furthermore, most prior work has measured gamma and alpha in separate paradigms or analyses (e.g., stimulus-optimization for gamma vs. covert attention for alpha), limiting direct comparisons under identical manipulations [18, 32, 39, 46, 47].

To address these questions, we directly compared the spatial and feature tuning of gamma and alpha oscillations in human visual cortex using EEG. By systematically varying retinotopic location, stimulus size, orientation, motion direction, and color, while also including no-stimulus baseline conditions, we tested whether gamma and alpha follow a shared tuning logic or instead reflect distinct encoding mechanisms. This approach allowed us to probe whether gamma's spatial specificity and feature selectivity [18, 32, 46] are mirrored by alpha's inhibitory footprint [30, 41, 50, 56], to quantify how anticipatory alpha suppression influences spatial summation [39, 47], and to reveal circumstances in which gamma–alpha relationships deviate from a simple inverse correlation [21, 35, 43]. The results, summarized below, provide new evidence for a tight but non-uniform coupling between feedforward-driven gamma synchronization and feedback-mediated alpha modulation.

Chapter 2

Literature Review

Understanding how the human brain processes visual information is central to neuroscience, with retinotopic mapping and orientation tuning serving as foundational concepts that define the organization of the visual cortex. Advances in neuroimaging techniques, including Electroencephalography (EEG), Magnetoencephalography (MEG), and functional Magnetic Resonance Imaging (fMRI), have played pivotal roles in revealing the mechanisms underlying these processes. This section discusses landmark studies that have contributed significantly to our understanding of visual processing in the brain.

2.1 Early Studies on Visual Cortex Organization

Hubel and Wiesel [23] mapped the functional architecture of the cat's visual cortex, identifying simple and complex cells (Figure 2.1). Simple cells have receptive fields with distinct excitatory and inhibitory regions, responding to specific orientations of light stimuli, while complex cells respond to oriented moving stimuli independent of precise position. They discovered a columnar organization in the visual cortex, where neurons within a column share orientation preference. Their findings established binocular interactions, showing that many neurons integrate signals from both eyes, crucial for depth perception. The study provided a hierarchical model of visual processing, where simple cells receive inputs from the lateral geniculate nucleus (LGN) and complex cells integrate signals across larger receptive fields. Their work revolutionized our understanding of cortical processing, laying the foundation for modern visual neuroscience.

2.2 Retinotopic Mapping in Humans

Sereno et al. (1995) used fMRI with phase-encoded retinal stimulation to map human visual areas (V1, V2, VP, V3, V4) noninvasively. They introduced a cortical

surface reconstruction method to precisely identify area borders using visual field sign analysis. Their study confirmed that human visual areas extend more anteriorly than in monkeys and emphasize central vision more strongly. The findings demonstrated that retinotopically organized areas overlap with regions involved in complex visual tasks, such as reading. This work pioneered high-resolution human retinotopic mapping, providing a critical foundation for functional neuroimaging and vision research [45].

Fang et al. [9] investigated orientation-tuned fMRI adaptation in the human visual cortex, demonstrating that fMRI responses in V1, V2, V3/VP, V3A, and V4 decrease with long-term adaptation, proportional to the angular difference between adapting and test stimuli (Figure 2.2). However, only V3A and V4 show this pattern with short-term adaptation.

2.3 Orientation Sensitivity and Radial Bias

Sasaki et al. [42] identified a radial orientation bias in the human and macaque visual cortex, where stimuli aligned radially to the center of gaze elicit stronger neural responses than tangential ones (Figure 2.3). Psychophysics and fMRI reveal that radial stimuli enhance contrast sensitivity and increase fMRI activity by approximately 20% in retinotopic regions. This bias is consistent across V1–V4 and higher visual areas, suggesting an evolutionarily conserved mechanism. The study establishes a neural link between orientation sensitivity and cortical retinotopy, challenging the assumption that orientation preferences are uniformly distributed across the cortex.

2.4 Gamma Oscillations and Neural Synchronization

Womelsdorf et al. [55] demonstrated that gamma-band synchronization (40–70 Hz) in V4 predicts reaction speed in a change detection task (Figure 2.4). Stronger gamma coherence before and after stimulus changes leads to faster responses, while synchronization to irrelevant stimuli slows reaction times. Trials with fast responses show higher gamma power and spike–field coherence, especially 350 ms before and 125 ms after stimulus changes. This synchronization reduces neuronal response latency, improving visuo-motor integration. The study highlights gamma-band activity as a key neural mechanism for attentional selection and behavioral efficiency.

Further research has explored the functional implications of this radial bias. For instance, a study published in the Journal of Vision investigated how radial orientation biases influence visual processing, finding that such biases modulate access to consciousness, with radial stimuli being more readily detected than tangential ones [22].

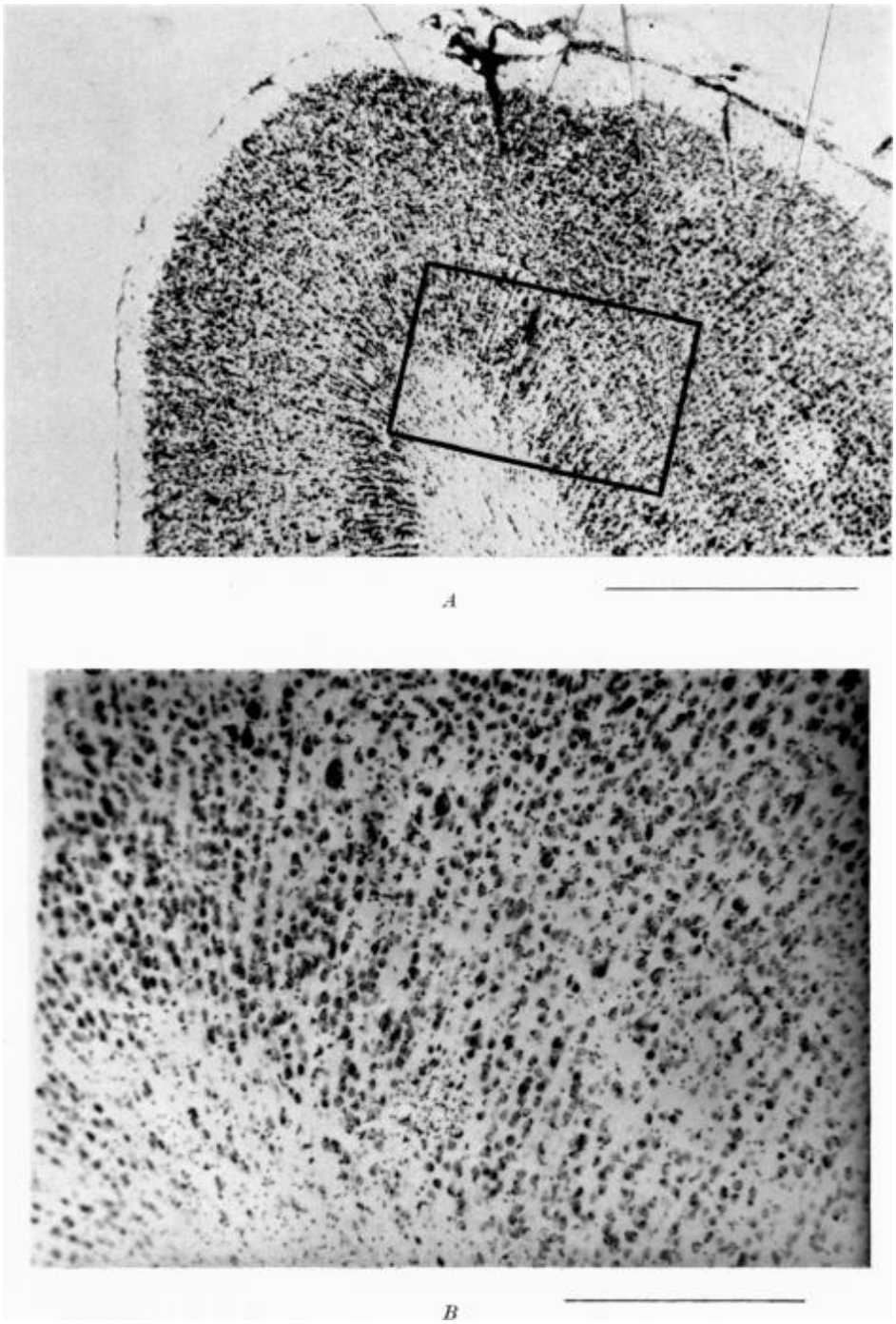

Figure 2.1: Classic examples of simple vs. complex receptive fields and columnar architecture.

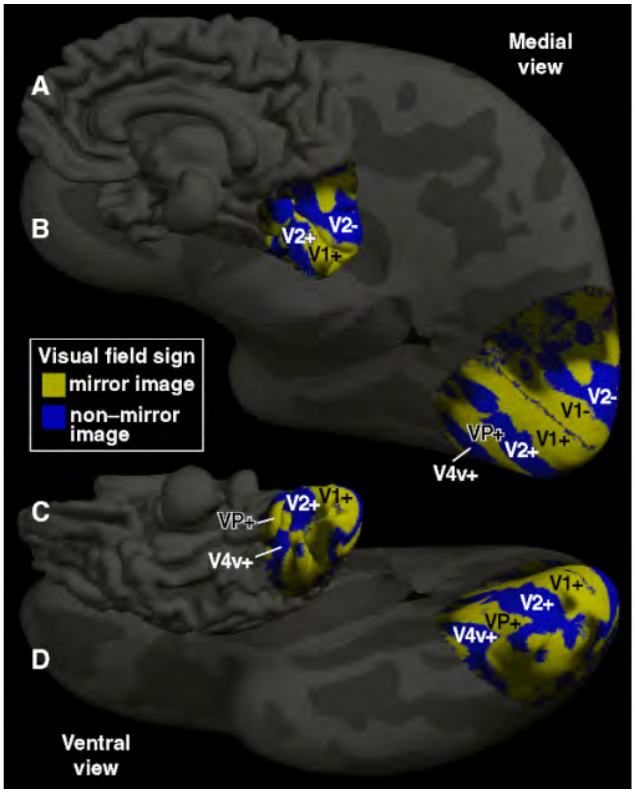

Figure 2.2: Orientation-tuned fMRI adaptation across visual areas.

Additionally, studies on orientation anisotropies in macaque visual areas have provided insights into how these biases affect visual perception and processing [8].

2.5 EEG Source Localization and Functional Resolution

Im et al. (2007) conducted a study to assess the spatial resolution of electroencephalography (EEG) cortical source imaging by comparing it with functional magnetic resonance imaging (fMRI)-based retinotopic mapping in the primary visual cortex (V1) (Figure 2.5). Im et al. [26] presented small circular checkerboard stimuli at various locations along the horizontal meridian and recorded both EEG and fMRI responses. The results demonstrated that EEG source localization closely matched fMRI activations, with a mean localization error of approximately 7 mm.

This error is smaller than the fMRI activation shift corresponding to a 3° change in the visual field (7.8 mm), indicating that EEG can accurately track small activation shifts in V1. These findings validate EEG as a reliable tool for studying early visual processing and highlight its ability to detect dynamic cortical changes with high spatial resolution [45].

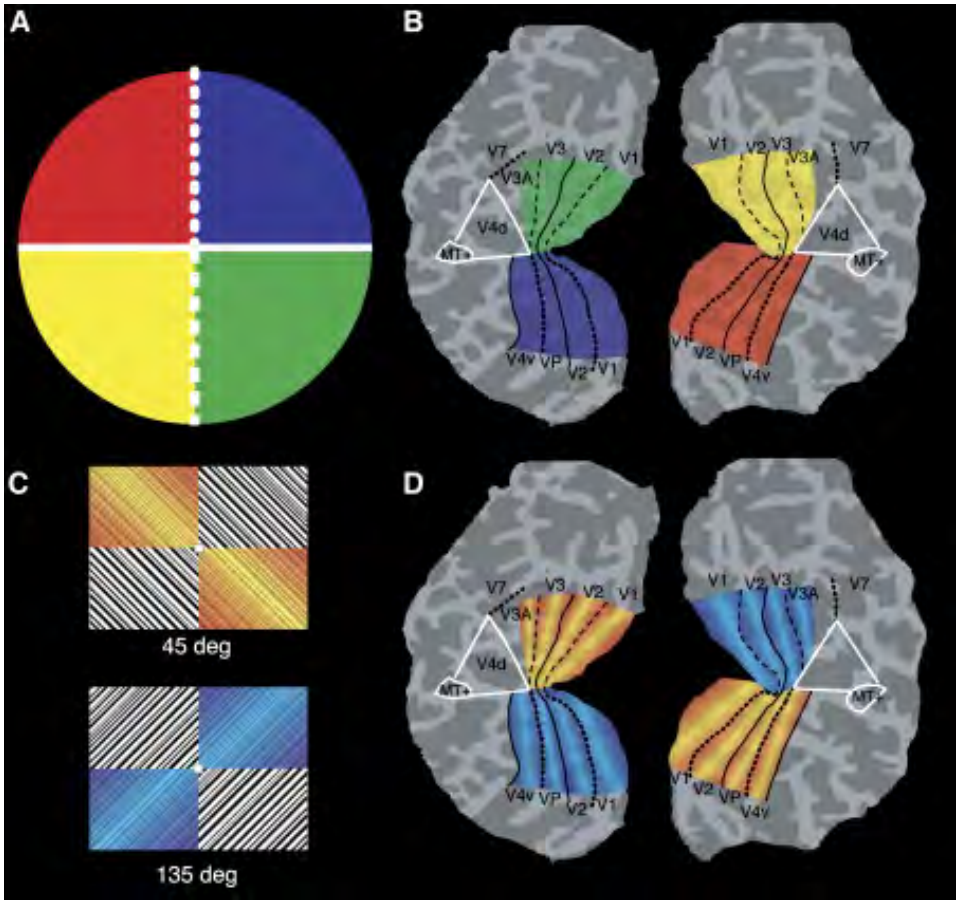

Figure 2.3: Radial orientation evokes stronger responses than tangential across visual areas.

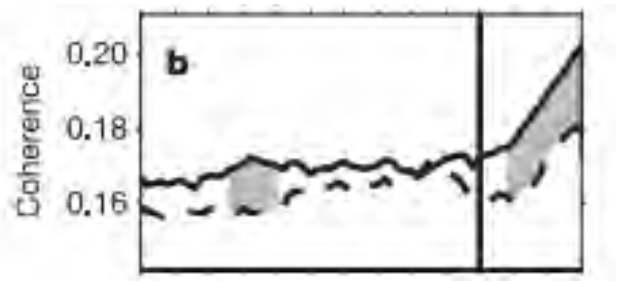

Figure 2.4: Gamma-band synchronization.

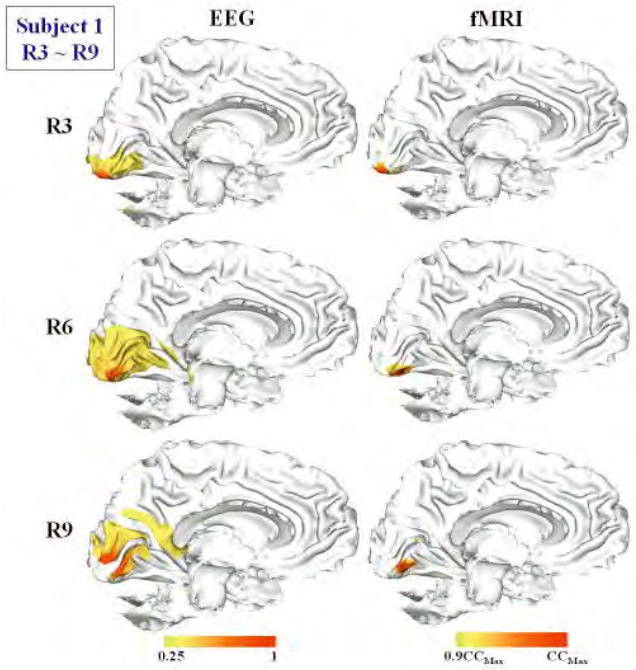

Figure 2.5: EEG cortical source imaging vs. fMRI retinotopy across right-hemisphere ROIs (R3–R9).

2.6 Alpha and Gamma Rhythms in Neural Processing

Jensen and Mazaheri (2010) proposed the rhythmic pulsing model, where alpha oscillations (8–12 Hz) periodically inhibit neural processing, shaping evoked responses (Figure 2.6). They introduced amplitude asymmetry, where alpha peaks and troughs are modulated differently, influencing slow cortical responses. Their findings challenge the additive and phase-resetting models, suggesting that stimuli are processed between alpha pulses rather than by a simple stimulus-driven activation. They developed the Amplitude Fluctuation Asymmetry Index (AFA) to quantify this effect, linking alpha modulation to sensory and cognitive processing. This model integrates alpha–gamma interactions, where gamma reflects active processing and alpha governs functional inhibition. Their framework unifies ongoing oscillatory activity, stimulus processing, and cognition, offering a new perspective on sensory gating and attention control [34].

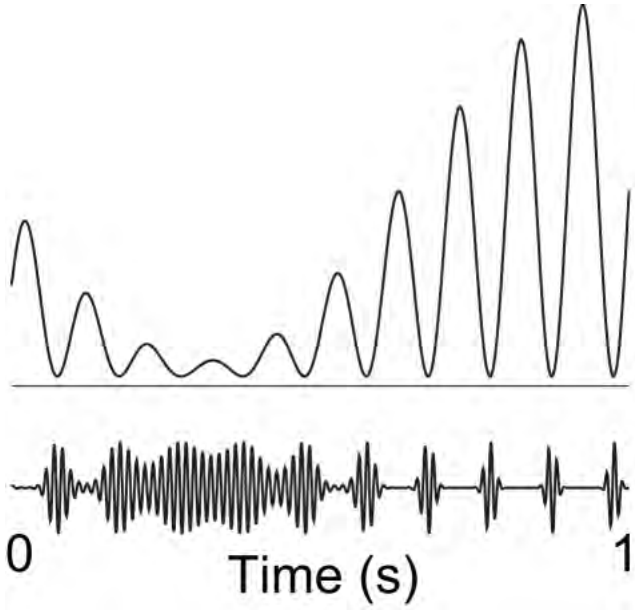

Figure 2.6: Alpha as rhythmic pulsing: inhibitory cycles gate processing; gamma bursts express computation within low-inhibition windows.

2.7 Feedforward and Feedback Processing

Gamma oscillations play a key role in neural communication and brain function. Higher gamma power enhances spike-field coherence, supporting signal transmission. Van Kerkoerle et al. [51] and Hakami et al. [19] showed that gamma (γ) oscillations (40–90 Hz) drive feedforward processing, while alpha (α) oscillations (8–12 Hz) mediate feedback in the monkey visual cortex (Figure 2.7). Layer-specific recordings reveal that γ-waves originate in layer 4 and propagate feedforward, whereas α-waves arise in superficial and deep layers and move in the feedback direction (Figure 2.8).

Microstimulation experiments confirm directionality, with V1 stimulation inducing γ in V4 and V4 stimulation eliciting α in V1. NMDA (N-Methyl-D-Aspartate) receptor blockers, known to reduce feedback effects, suppress α while enhancing γ, reinforcing this model. These findings establish α-γ interactions as key markers of hierarchical communication in sensory processing and cognitive control. Further studies demonstrate that gamma-modulated spiking activity in V1 predicts V1-V2 coupling better than V2 gamma rhythms, suggesting that feedforward synchronization underpins cortical communication [29].

Ichim et al. [24] propose the GAMER hypothesis, positioning gamma rhythms as fundamental for neurovascular regulation and brain homeostasis. Their findings indicate that gamma oscillations sustain neural circuits and cognition, with

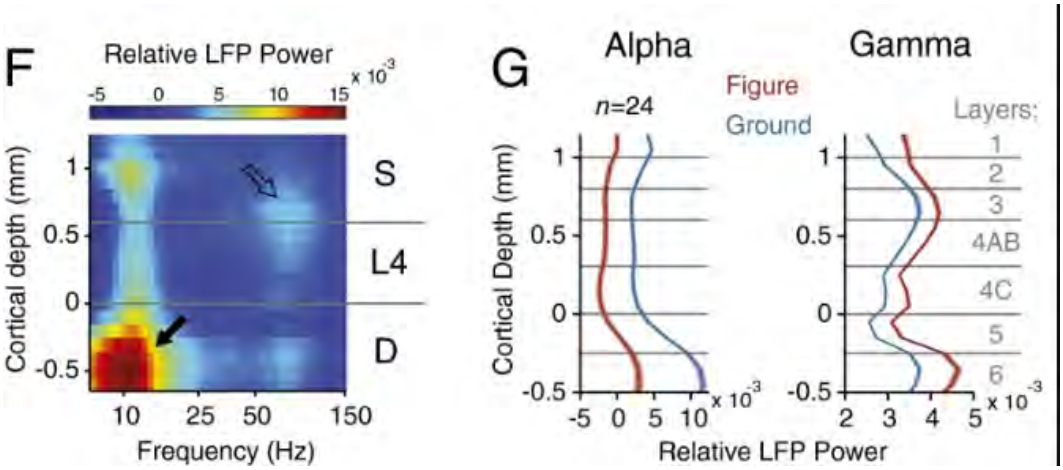

Figure 2.7: Laminar profiles: γ peaks in L4 (feedforward); α/β are stronger in superficial/deep layers (feedback).

applications in GENUS (Gamma Entrainment Using Sensory Stimulation) for neurodegenerative conditions. These findings support the idea that gamma oscillations coordinate inter-area communication, while alpha suppression modulates sensory gating. The hierarchical organization of alpha and gamma rhythms highlights their complementary roles in visual perception, with gamma encoding stimulus details and alpha optimizing processing efficiency [40].

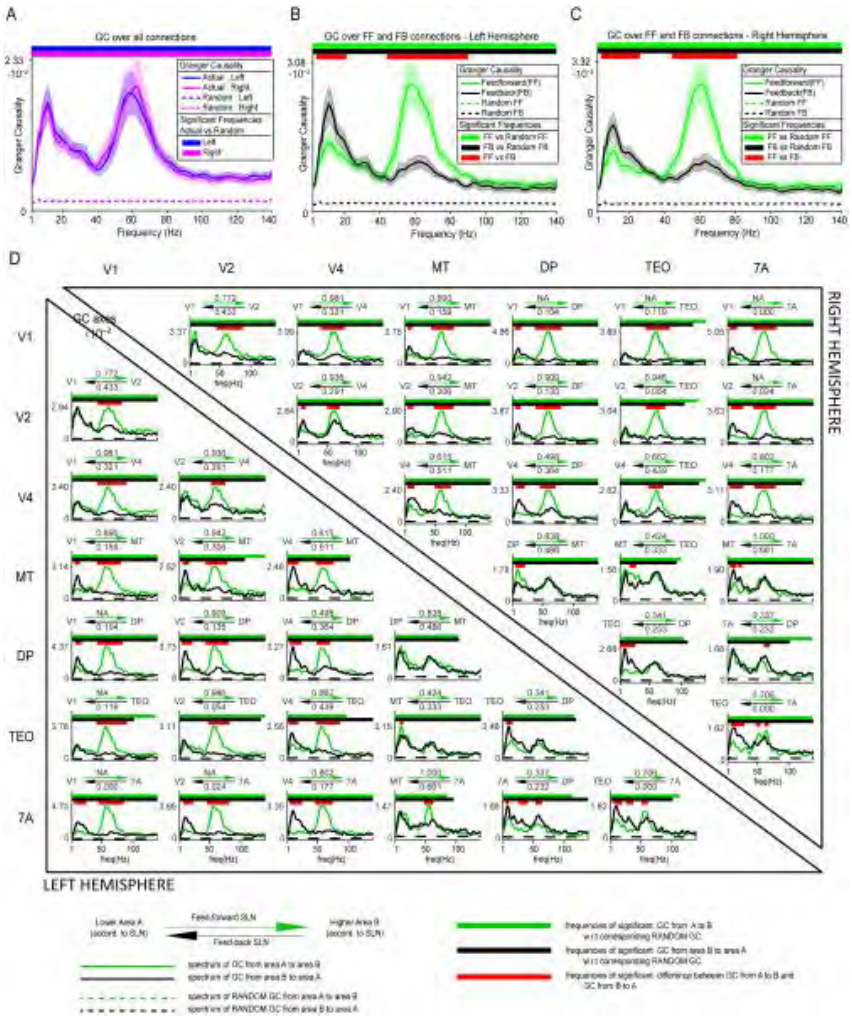

Figure 2.8: Frequency-resolved directed influences: γ dominates feedforward, while α/β dominate feedback between human visual areas.

Chapter 3

Materials and Methods

3.1 Subjects

Thirty healthy young adults (17 male, 13 female; age range 18–38 years) were recruited from the Bishop's University and Université de Sherbrooke communities. All participants provided written informed consent in accordance with ethics approval from the Centre intégré universitaire de santé et de services sociaux de l'Estrie – Centre hospitalier universitaire de Sherbrooke (CIUSSS de l'Estrie – CHUS). All methods were performed in accordance with the relevant guidelines and regulations. Participants were screened to exclude any neurological or psychiatric disorders, sleep disorders, or use of medications affecting the central nervous system.

3.2 Stimulus Presentation

Stimuli were generated in MATLAB (The MathWorks, Inc., Natick, MA) using Psychophysics Toolbox extensions and presented on a 15-inch CRT monitor in a dimly lit, sound-attenuated room. The display background was uniform gray, with luminance matched to the mean luminance of each stimulus. The grating stimuli (both bars and annulus) had a spatial frequency of 3 cycles/° and a temporal frequency of 6 cycles/s; the full-field stimulus had an aperture width of 10° diameter centered on fixation.

The stimulus set consisted of 36 distinct trigger types (see Figures 3.1 to 3.3).

- **Retinotopic mapping stimuli:** full-field; left/right hemifields; upper/lower hemifields; four quadrants; eight octants; central fovea; peripheral ring; and a blank "anticipatory" condition with no visual stimulus. Retinotopic masks were applied to a 100% contrast inward-drifting circular annulus.

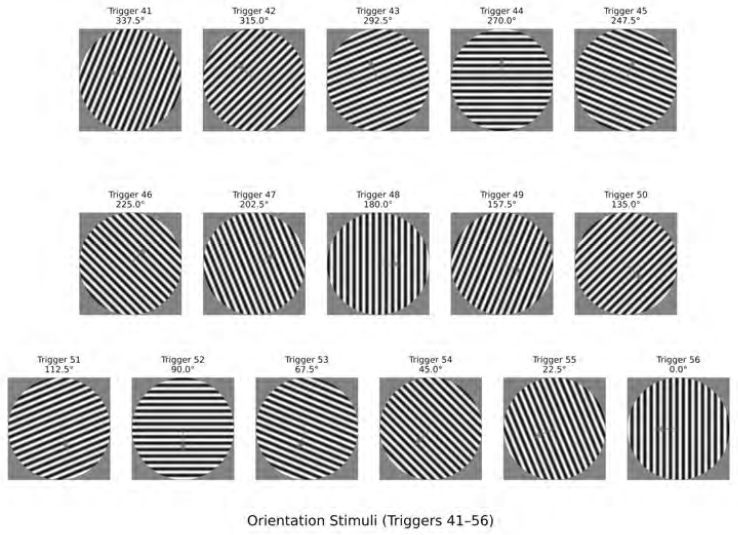

Figure 3.1: Stimulus design showing the combination of orientation, motion direction, and visual hemifield.

- **Orientation stimuli:** sixteen high-contrast drifting gratings, starting at vertical (0°) drifting leftward, rotated in 22.5° increments through 337.5°. Motion was always orthogonal to the grating orientation.

All stimuli were presented at 100% Michelson contrast against the gray background. Retinotopic stimuli were spatially masked using binary apertures smoothed with a Gaussian edge, while orientation stimuli were unmasked except for the circular aperture.

Each trial began with a fixation period in which a black crosshair was presented. Immediately before stimulus onset, the crosshair turned red for a randomized foreperiod of 0.25 ± 0.15 s, serving as a temporal cue that the stimulus would appear. This red "primer" was also used before blank trials in the anticipatory condition. Stimuli were then displayed for 3 s, followed by a 1 s post-stimulus fixation interval before the next trial began.

Stimuli were presented in "batches" of 8 minutes, with participants maintaining central fixation throughout each batch and given 1–2 min rest periods between. Stimuli were presented in pseudorandom order, with 10–20 repetitions per stimulus type (360–720 total trials per participant). The total session lasted approximately 1 hour.

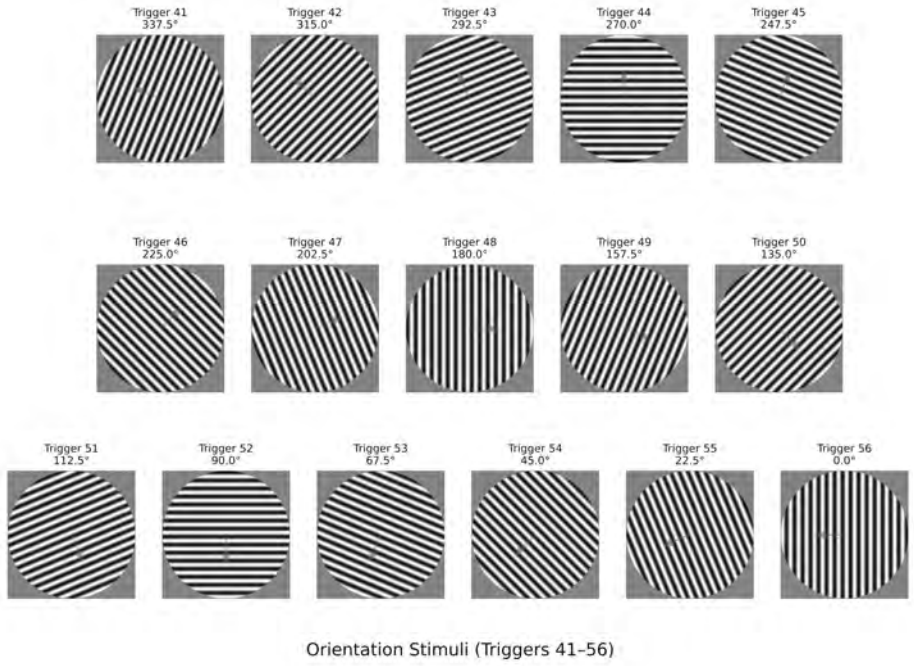

Figure 3.2: Orientation stimuli (stimulus images only). Sixteen high-contrast drifting gratings from 0° to 337.5° in 22.5° steps; motion was orthogonal to orientation.

3.3 EEG Preprocessing – Independent Component Analysis (ICA) Extraction

Continuous EEG data were acquired in BrainVision format (`.vhdr`) and preprocessed using MNE-Python (v1.8.0) with the Picard ICA algorithm (Picard v0.8). All preprocessing was performed in Python (v3.9.21).

Each `.vhdr` file was imported using `mne.io.read_raw_brainvision()` with data preloaded into memory. To identify bad channels, the raw signal was band-pass filtered between 10–100 Hz (FIR filter, firwin design) and the sum of squared differences (SSD) was computed for each channel. Z-scores of SSD values were calculated, and channels with $z > 1$ were marked as bad and subsequently interpolated using spherical spline interpolation, resulting in the removal of approximately 1–3 channels per subject.

Line noise was removed using a 60 Hz notch filter, and a copy of the data was then band-pass filtered between 1–100 Hz (firwin design) for ICA (Independent Component Analysis). This filtered dataset was resampled to 200 Hz to reduce computational load. Events were extracted from annotations, and epochs were defined from −1.0 s to +4.0 s relative to event onsets and concatenated into a

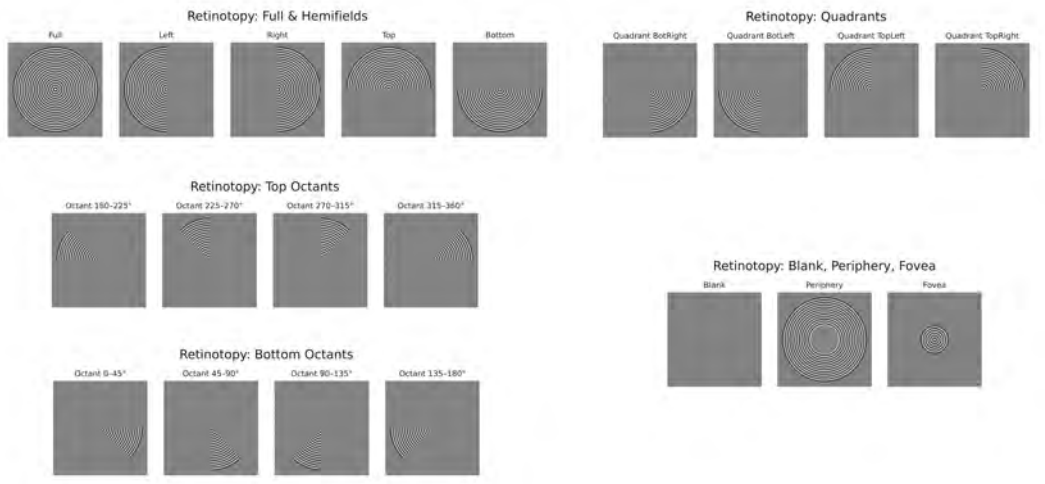

Figure 3.3: Retinotopy stimuli (stimulus images only). Panels show the masks used for full-field, hemifield, quadrant, octant (0°–180°; 180°–360°), foveal/peripheral, and blank conditions. All stimuli appeared at 100% contrast on a gray background with central fixation.

continuous `Raw` object for ICA training.

ICA was performed using the Picard algorithm with the following parameters: `n_components=60`, `extended=True`, `max_iter=500`. The ICA model was fit to the concatenated epochs, and the resulting decomposition (unmixing and mixing matrices, component activations) was saved in `.fif` format for later use in artifact identification and removal.

3.4 Artifact Identification and Removal

For each component, the mean ERSP (Event-Related Spectral Perturbation) across trials was visualized alongside its corresponding scalp topography derived from the ICA weight matrix. Components were manually inspected and classified based on both their spectral and spatial profiles. Components showing narrowband gamma activity (30–100 Hz) with posterior scalp topographies, as well as those with narrowband alpha activity (8–12 Hz), were retained for further analysis. All selected "good" components were saved in subject-specific files for use in subsequent stages of signal reconstruction and analysis, typically 3–5 components were retained per subject.

The saved ICA solution was then used to extract source activations for only the retained components. Event-locked epochs (−1.6 s to +4.6 s, including a 0.6 s buffer) were segmented from these sources for all stimulus triggers of interest.

Time–frequency representations (4–100 Hz) were computed using Morlet wavelet convolution, cropped to the analysis window (−1.0 s to +4.0 s) to remove padding, and log-transformed. Single-trial baseline correction was performed for each component and frequency bin using the mean power from −0.5 s to 0 s pre-stimulus, producing baseline-normalized ERSPs for every trial, component, and frequency–time bin. These single-trial ERSPs were then stored for each subject along with their corresponding stimulus IDs, enabling both subject-level and stimulus-level averaging in later analyses.

3.5 Orientation Tuning Analysis

Orientation tuning analyses were performed on baseline-corrected, single-trial ERSPs from all retained ICA components across subjects. To isolate trials corrupted by broadband muscular or ocular artifacts, we first extracted log power in the 80–100 Hz band (broadband gamma) for each trial. The maximum power within the analysis window (0–3 s) was computed per trial, and values were z-scored across all subjects. Trials with $|z| > 4$ were excluded to remove extreme outliers (the same procedure was applied in the retinotopy analysis).

A two-dimensional repeated-measures approach was used to assess orientation selectivity. First, all single-trial ERSPs were Gaussian-smoothed ($\sigma = 2$ frequency bins, 4 time bins) to increase spatial coherence. A pointwise one-way ANOVA (factor: stimulus identity) was then conducted across all grating orientations for each frequency–time bin, yielding F- and p-value maps. p-values were transformed to $-\log_{10}$ scale, and significant clusters ($p < 0.01$, cluster-based spatial connectivity) were identified using an 8-connected neighborhood criterion. The size and location of significant clusters were visualized, and mean ERSP values within these clusters were extracted per stimulus type. Cluster-averaged ERSPs were compared across orientations using bar plots (mean ± SEM).

Stimuli were further binned into predefined orientation and motion-direction categories (e.g., “cardinal,” “oblique ±22.5°,” “vertical,” “horizontal,” “left,” “right,” “up,” “down”). Within each bin, mean gamma power (40–80 Hz, 0–3 s) and alpha power (8–15 Hz, 0–3 s) were computed, along with standard errors. Pearson correlations between bin-averaged alpha and gamma power were calculated separately for orientation bins and for direction bins; linear fits were overlaid on scatter plots with correlation coefficients (r) and p-values reported.

To examine pairwise differences between bins, two-sample Welch’s t-tests were performed on the trial-level alpha and gamma values for each bin combination. This produced t-value and p-value matrices for both orientation and direction conditions, which were visualized as lower-triangular heatmaps with p-values displayed in each cell and significance denoted by an asterisk ($p < 0.05$). Finally, a frequency×frequency correlation matrix (Pearson’s r) was computed from the mean post-stimulus (0–3 s) power spectra across all trials.

3.6 Computation of Per-Electrode Power

For each subject, cleaned EEG data were reconstructed in sensor space by loading the subject's saved ICA decomposition, marking all components not in the good-component list for exclusion, and applying the ICA to the continuous EEG, thereby removing artifactual sources while retaining physiologically meaningful activity. The cleaned scalp-space EEG was segmented into epochs time-locked to each stimulus (−0.5 to 3.5 s), and narrowband alpha (8–13 Hz) and gamma (40–80 Hz) signals were isolated by applying zero-phase FIR band-pass filters to separate copies of the data. For each trial, absolute analytic amplitude was computed at every electrode, and the mean amplitude in the stimulus window (0–3.0 s) was compared to the mean amplitude in the pre-stimulus baseline (−0.5–0 s). The final power measure at each electrode was the difference between these two means, expressed as |task| − |baseline|. This computation was performed separately for alpha and gamma, averaged across trials within each stimulus type, and stored both as trial-level arrays and as per-stimulus, per-channel matrices.

3.7 Topographic Visualization of Alpha and Gamma Power

To display spatial distributions of stimulus-evoked power, electrode coordinates were extracted from a representative subject's EEG montage and projected to 2-D using spherical coordinates. Channels with poor coverage or located at the extreme periphery (e.g., mastoid, inferior temporal) were excluded to improve interpolation stability. For each stimulus type, the mean alpha or gamma difference values across subjects were interpolated over a 2-D grid using radial basis functions (multiquadric kernel, smooth = 0.1). The interpolation grid was circularly masked to match the scalp outline, with a slightly expanded radius to ensure outermost electrodes were represented.

3.8 Retinotopy analysis

Retinotopy figures were generated from the same baseline-corrected, single-trial ERSP datasets described earlier, using all retained ICA components. Band-specific power measures were computed by averaging over both time (0–3 s) and the relevant frequency range—8–15 Hz for alpha, 40–80 Hz for gamma. Mean and SEM values were calculated for each stimulus, and results were summarized in bar plots for each band. Alpha and gamma means were then compared directly in a scatter plot with a least-squares regression fit, reporting correlation coefficients and p-values, and residuals from the regression were plotted to highlight stimuli deviating most from the alpha–gamma relationship. Figure 3.4 shows the full set of 16 oriented grating stimuli (Triggers 41–56), spaced at 22.5° intervals from 0° (vertical) to 360°,

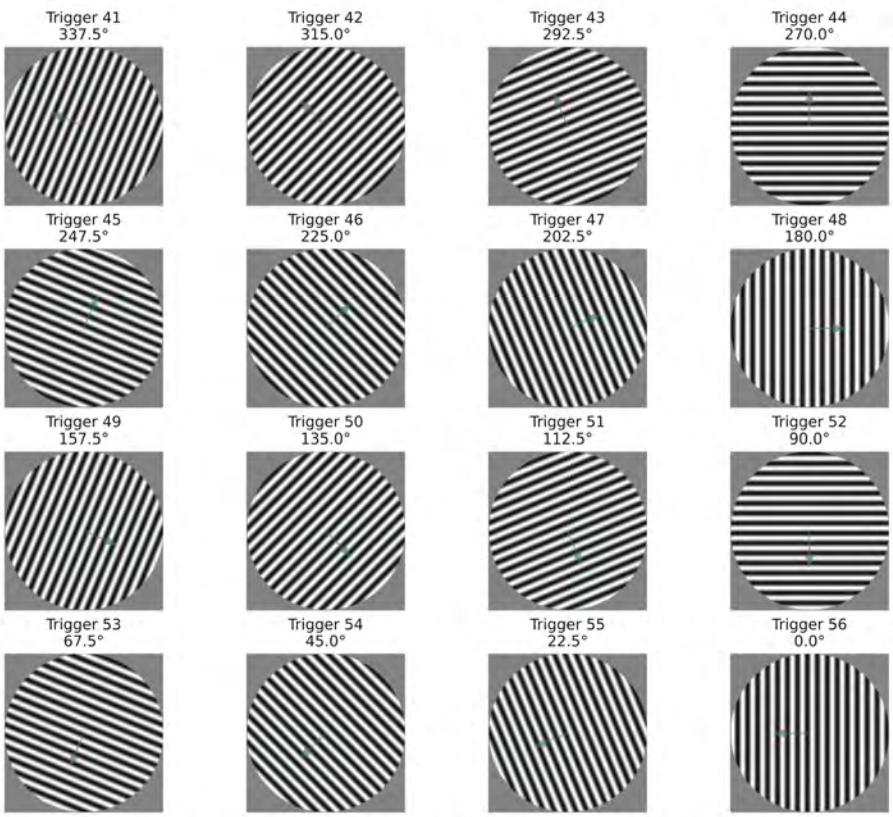

Figure 3.4: Sixteen oriented grating stimuli (Triggers 41–56) spaced at 22.5° intervals from 0° to 360°.

covering cardinal, oblique, and intermediate directions. These stimuli served as the basis for comparing evoked spectral responses across orientations.

3.9 Retinotopic Group Comparisons and Model Fits

To examine spatial summation properties, stimuli were grouped into standard retinotopy configurations: left vs. right hemifields, upper vs. lower hemifields, quadrants, octants, and fovea vs. periphery. For each grouping, the full-field stimulus spectrum was compared to (a) the spectra for each part stimulus, (b) the sum of the part spectra, and (c) the sum of the part spectra with the blank-field (no-stimulus) spectrum subtracted. These quantities were overlaid in line plots to visualize how closely part-sum responses matched the full-field response.

Quantitative model fitting then compared two summation models—a simple linear sum and a divisive normalization (DivNorm) model with fixed $\sigma = 0.5$—applied separately to alpha and gamma responses. For each grouping, mean absolute errors (MAE) between model predictions and the observed full-field response were computed, with an additional variant for alpha in which the mean blank-stimulus power was subtracted prior to fitting. These errors were summarized in grouped bar charts for each band and model type, enabling direct visual comparison of linear versus normalized summation performance across retinotopic configurations.

3.10 Per-Electrode Statistical Mapping of Retinotopic Effects

Per-electrode one-way ANOVAs were performed across the grouped conditions; for the special "Blank $\neq 0$" test, a per-electrode one-sample t-test against zero was used. The resulting p-values were converted to $-\log_{10}(p)$ for visualization.

Chapter 4

Results

This chapter presents the main experimental results, divided into two major sections: (1) Retinotopy analyses and (2) Orientation analyses. Each section includes both qualitative and quantitative components. Qualitative analyses describe the general spectral and topographic patterns, while quantitative analyses report the statistical outcomes and model-based interpretations.

4.1 Retinotopy Analyses

4.1.1 Retinotopy: Qualitative Results

The spectral and topographical analyses in Figure 4.1A revealed robust stimulus-induced gamma-band (40–100 Hz) increases and alpha-band (8–12 Hz) decreases following stimulus onset across all trials. These responses were temporally aligned with visual presentation (time 0) and showed distinct spatial distributions. Gamma-band power was maximal over occipital electrodes, indicating localized visual cortex activation, while alpha suppression extended broadly across posterior scalp regions, consistent with desynchronization during visual engagement.

Figure 4.2 qualitatively demonstrates the spatial specificity of induced oscillations across retinotopic stimuli. Full-field and hemifield stimulation elicited the strongest gamma responses for full and lower field stimuli, consistent with the anatomical overrepresentation of the lower visual field in primary visual cortex.

In Figure 4.3, quadrant stimuli produced distinct topographic gamma patterns: lower-left and lower-right quadrants showed strong focal activation in contralateral occipital areas, whereas upper quadrant responses were weaker and more diffuse.

Figure 4.4 further refines these findings with octant-level resolution, showing that bottom-octant stimuli consistently produced the largest gamma increases, especially between 90°–135° and 135°–180°, whereas top-octant responses were notably weaker.

Figure 4.5 revealed that the “Blank” condition evoked negligible gamma power

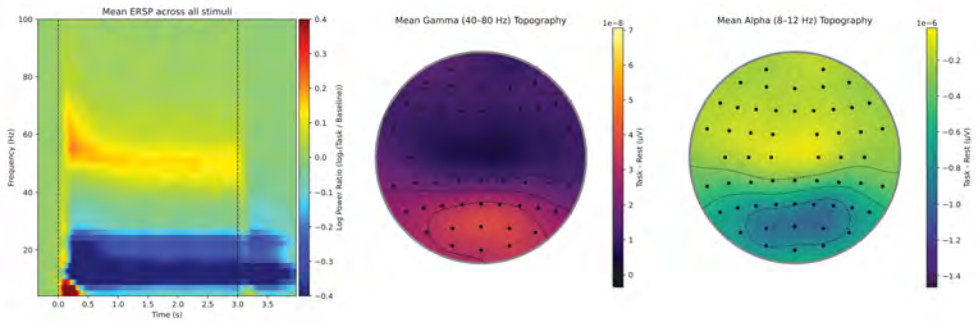

Figure 4.1: Time–frequency plots and topographic maps for gamma (40–100 Hz) and alpha (8–12 Hz) bands.

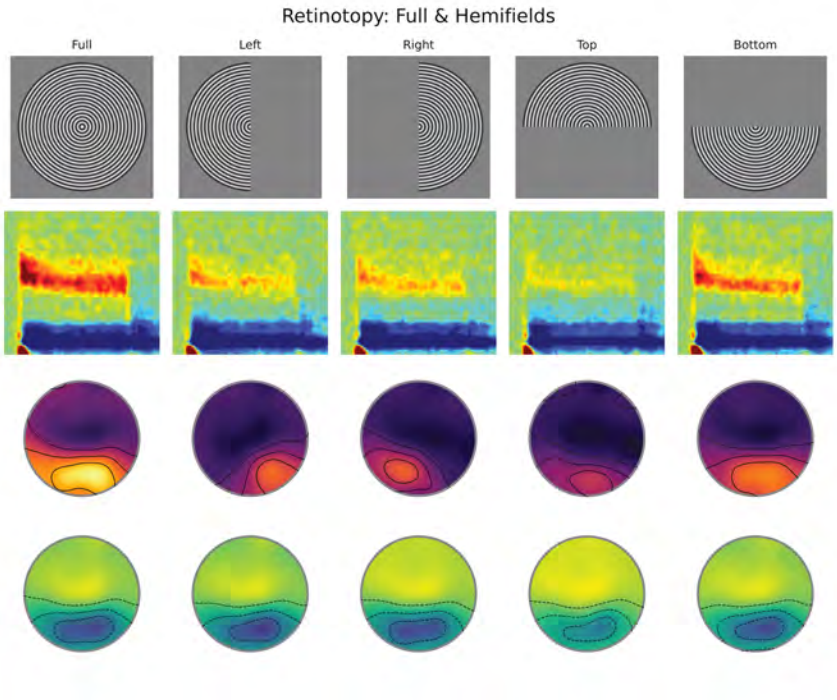

Figure 4.2: Topographic maps for full-field and hemifield stimuli.

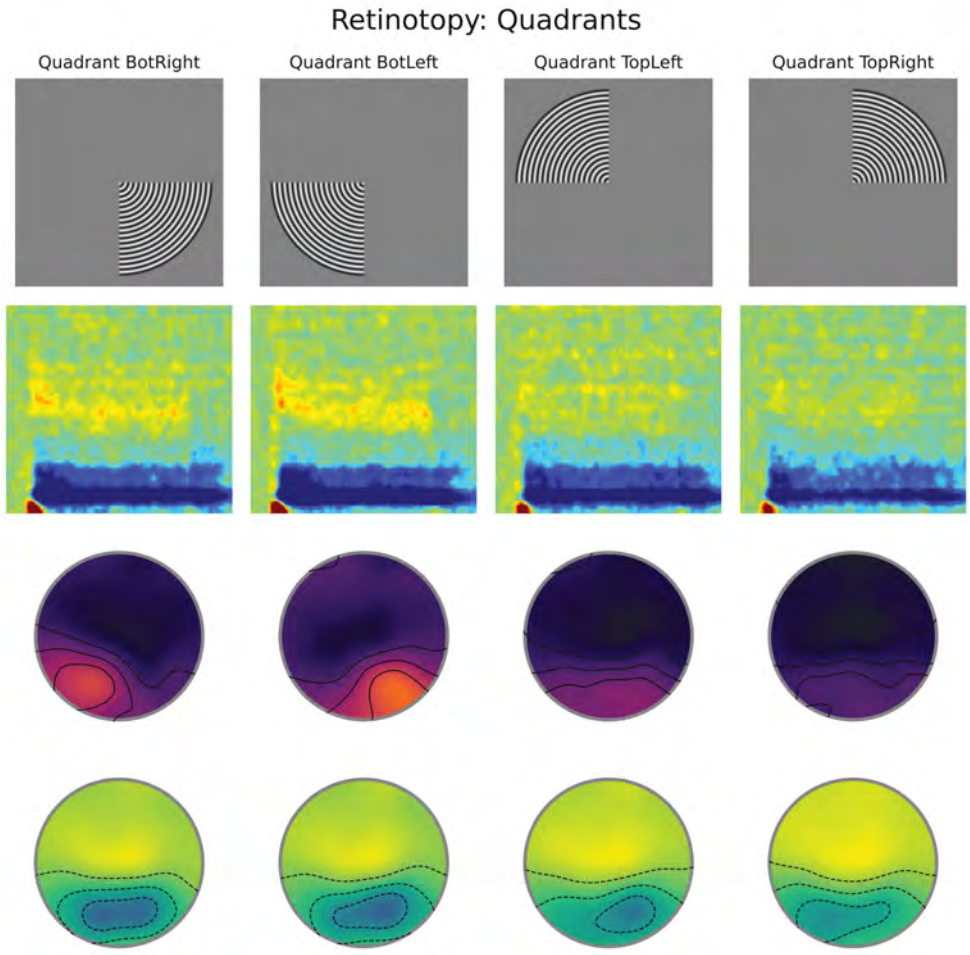

Figure 4.3: Topographic maps for quadrant stimuli.

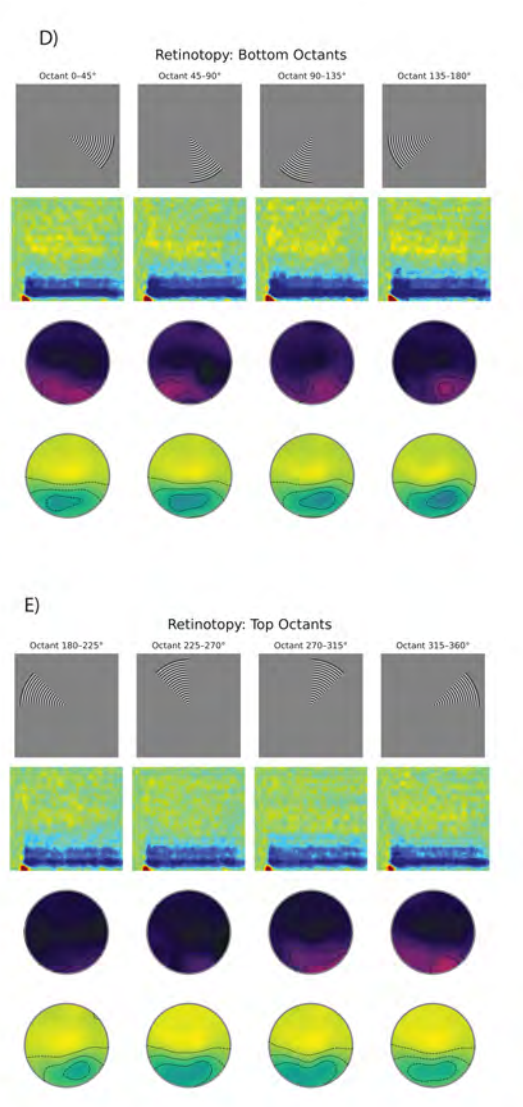

Figure 4.4: Topographic maps for octant stimuli (0°–360°).

but strong post-stimulus alpha responses, while peripheral and central stimuli showed distinct spatial patterns peripheral stimulation activated lateral occipital sites, whereas foveal stimulation produced focal midline gamma.

4.1.2 Retinotopy: Quantitative Analysis

Figure 4.6 displays the scalp-wise $-\log_{10}(p)$ maps from ANOVAs and t-tests comparing per-electrode gamma and alpha power across retinotopic groupings. Gamma responses showed robust spatial selectivity, with significant clusters ($p < 0.01$) in occipital regions, whereas alpha responses exhibited weaker spatial differentiation.

Figure 4.7 summarizes induced band power (0–3 s) across all conditions. Gamma power was strongest for full-field and lower-field stimuli, while alpha suppression followed a similar pattern, leading to a significant inverse correlation ($r = -0.84$, $p < 0.0001$).

Figure 4.8 compares full-field spectra with summed subfield responses, demonstrating near-linear summation for gamma and subadditive (nonlinear) suppression for alpha, consistent with divisive normalization.

Figure 4.9 confirms that gamma power fits a linear model, whereas alpha suppression follows a divisive normalization pattern with lower model errors.

4.2 Orientation Analyses

4.2.1 Orientation: Qualitative Results

Figure 4.10 shows gamma responses across 16 oriented grating stimuli. All orientations produced similar temporal gamma profiles but with topographic variability across angles (e.g., 45°, 90°, 135°). Alpha suppression remained consistent, suggesting it reflects general visual engagement rather than orientation tuning.
Figure 4.11 presents one-way repeated-measures ANOVA results showing orientation sensitivity in gamma-band power but not alpha-band. Cluster-based permutation tests revealed a significant gamma cluster ($p < 0.01$).

4.2.2 Orientation: Quantitative Analysis

Figure 4.12 quantifies power modulation for orientation and drift direction. Gamma power peaked for oblique orientations (112.5°–135°), while alpha suppression was strongest for cardinal orientations. A strong positive correlation ($r = 0.94$, $p < 0.005$) was observed across orientations, reversing the inverse relationship seen in retinotopy.

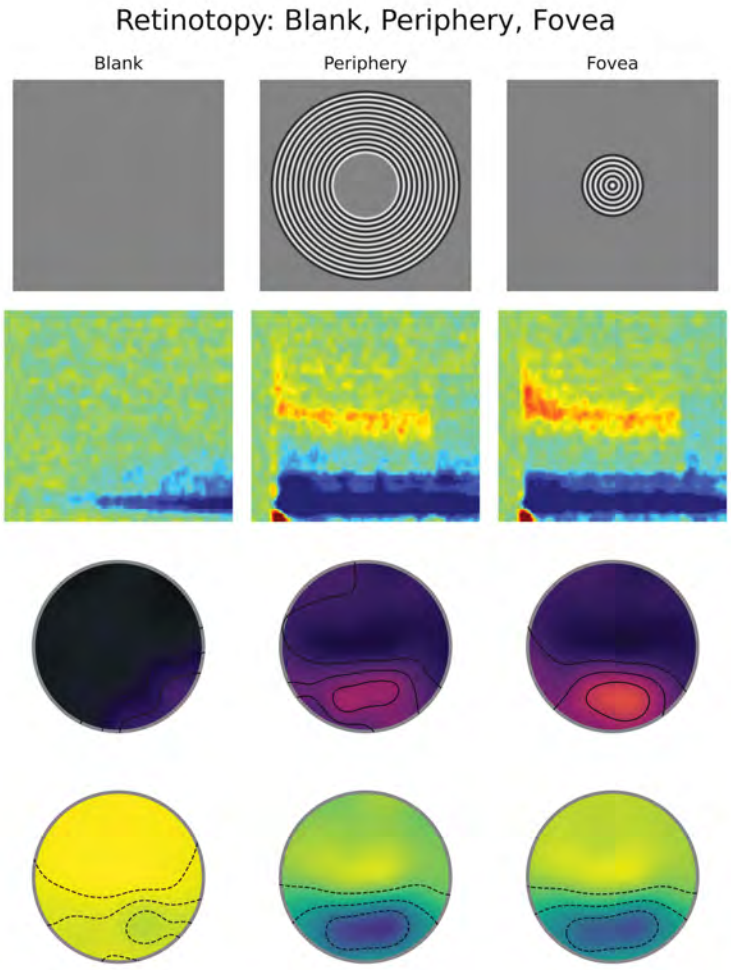

Figure 4.5: Topographic maps for blank, foveal, and peripheral stimuli.

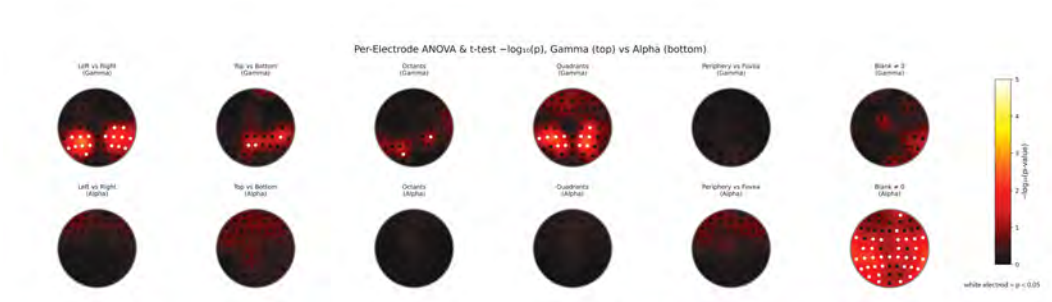

Figure 4.6: Scalp-wise $-\log_{10}(p)$ maps from ANOVAs and t-tests for gamma (top) and alpha (bottom) across retinotopic groupings.

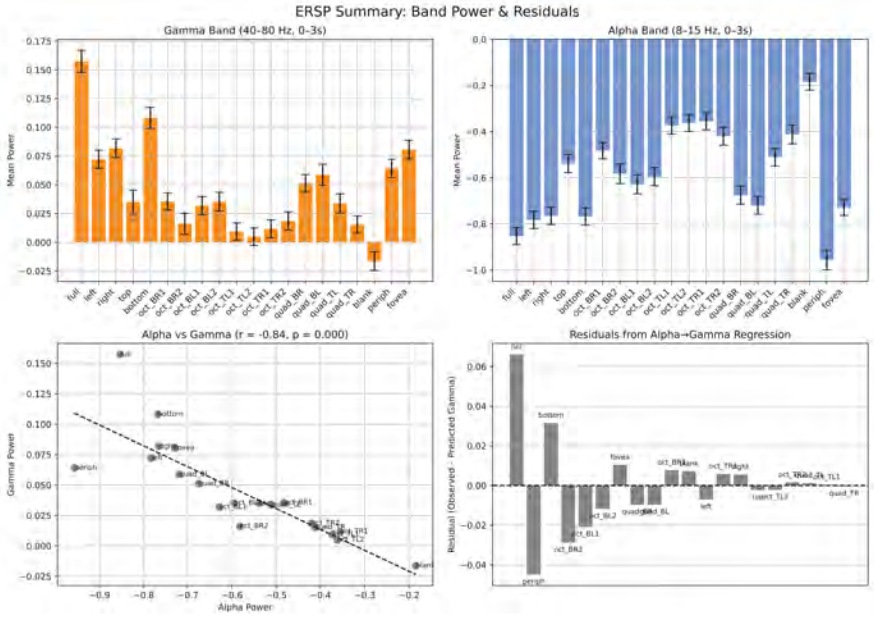

Figure 4.7: Band-power summaries and scatterplot of alpha vs. gamma power across retinotopic conditions.

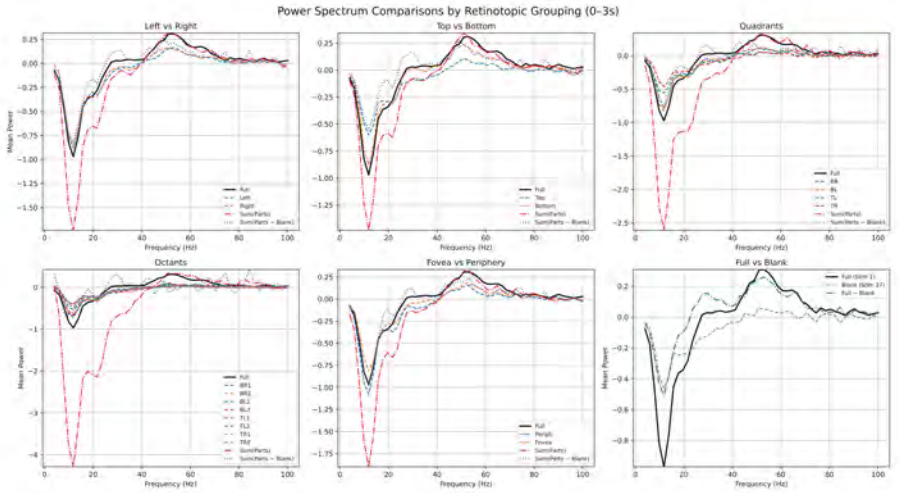

Figure 4.8: Full-field spectra vs. summed subfield responses for gamma and alpha across groupings.

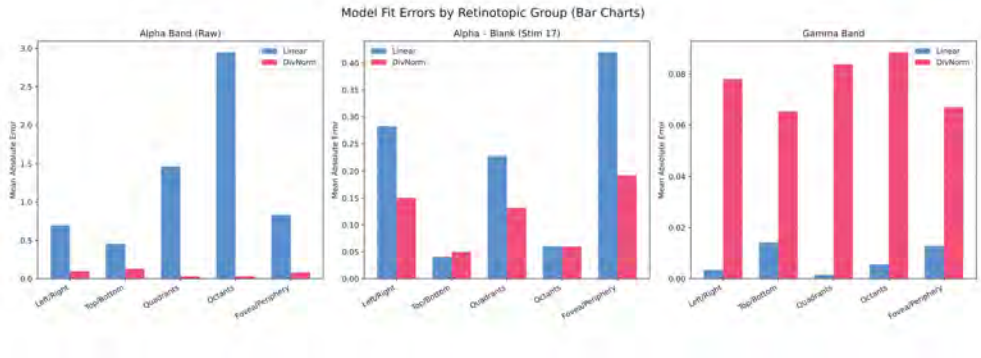

Figure 4.9: Model prediction errors for linear vs. divisive normalization fits for alpha and gamma bands.

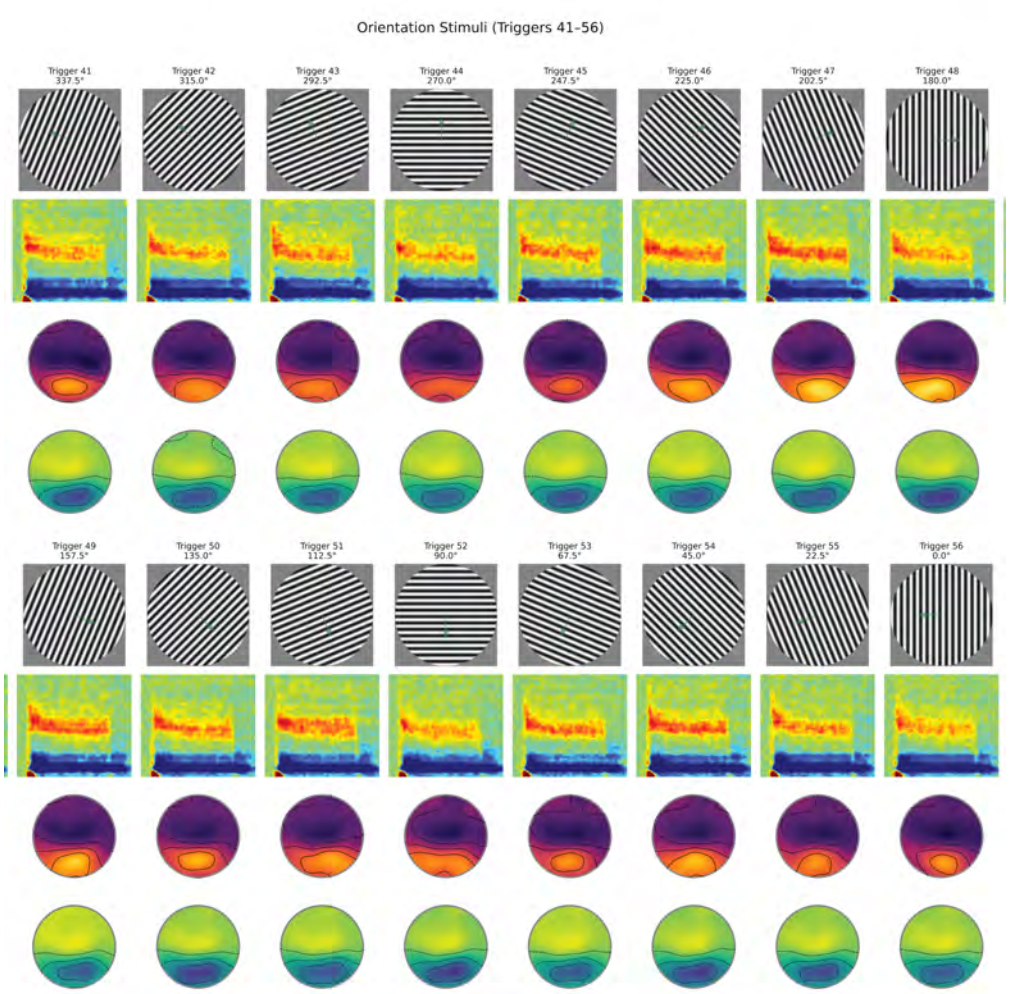

Figure 4.10: Time–frequency plots and topographic maps for 16 oriented grating stimuli.

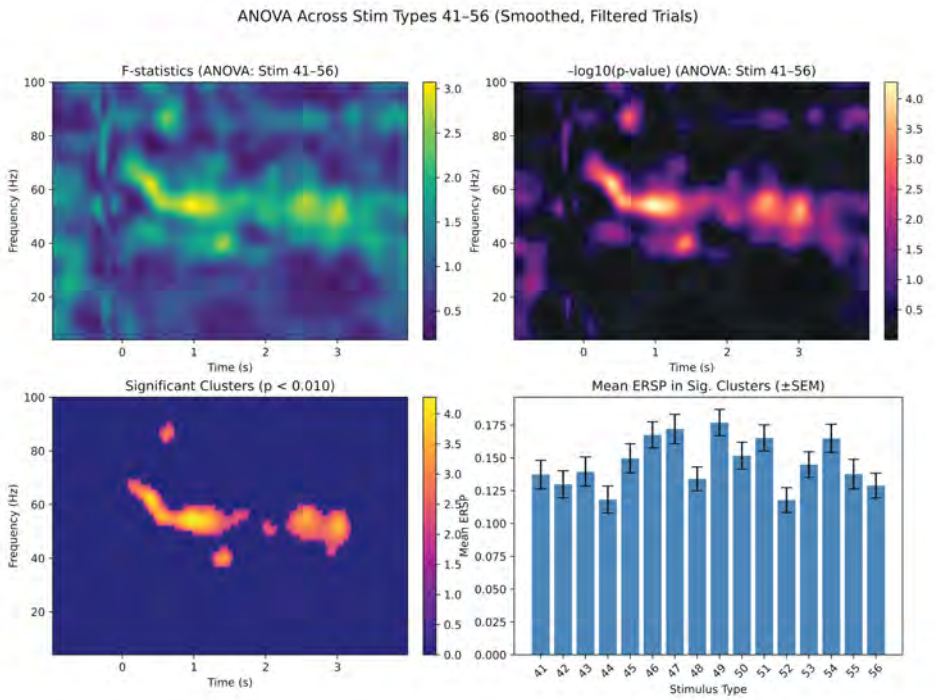

Figure 4.11: One-way repeated-measures ANOVA results and cluster-based permutation tests for orientation sensitivity.

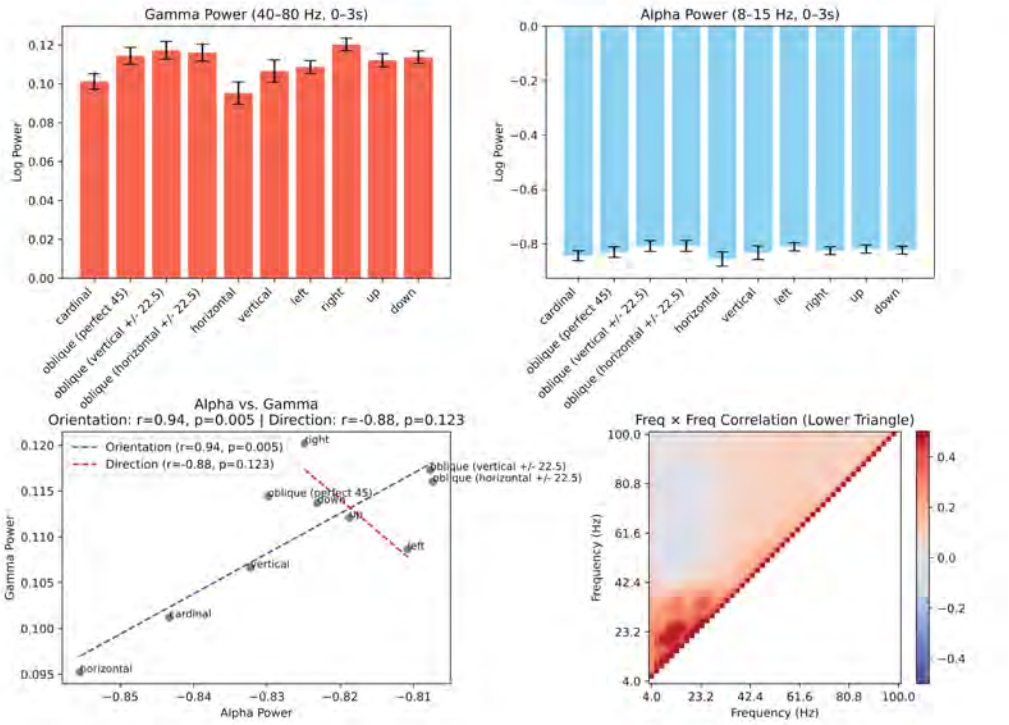

Figure 4.12: Band-power summaries for gamma and alpha across orientations and drift directions, with correlation matrices.

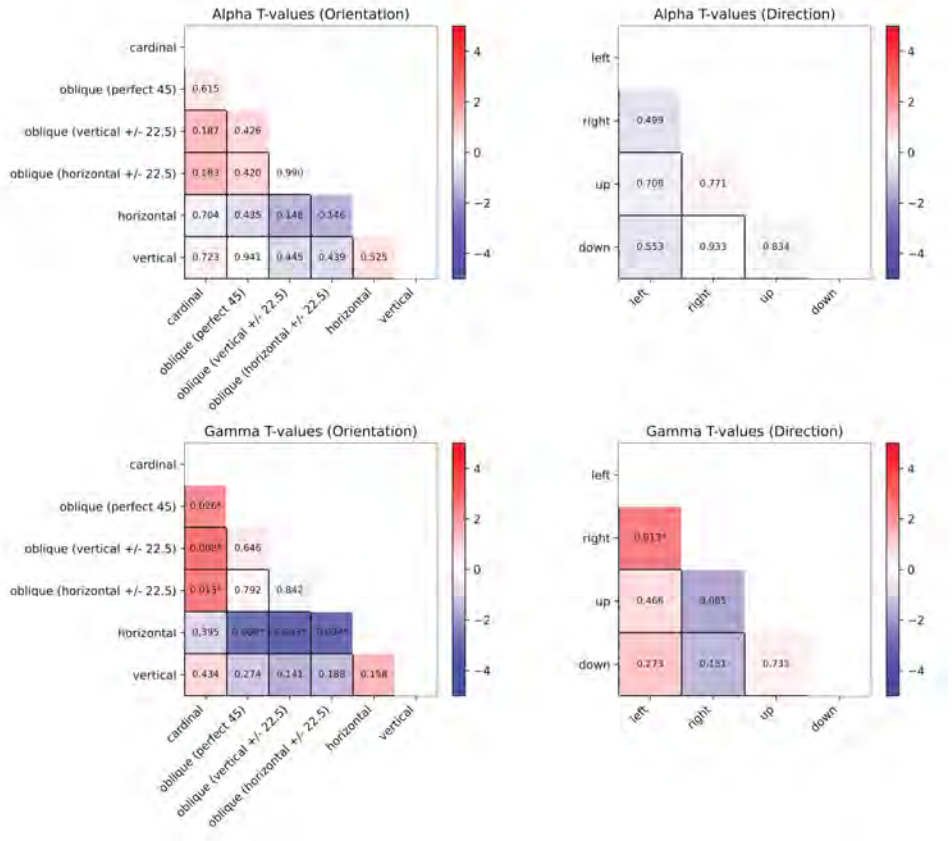

Figure 4.13: Pairwise t-test results for orientation and drift direction effects in alpha and gamma bands.

Figure 4.13 explores orientation and directional effects using pairwise t-tests. Gamma showed significant tuning for oblique vs. cardinal angles ($p < 0.01$), whereas alpha exhibited only modest trends.

Summary: Together, these findings demonstrate that gamma activity reflects localized feature-specific processing (orientation and spatial tuning), while alpha suppression indicates a broader, non-specific engagement of visual networks. Gamma behaves linearly with spatial integration, whereas alpha follows divisive normalization, suggesting distinct computational roles for these rhythms in visual coding.

Chapter 5

Discussion and Conclusion

5.1 Discussion

The findings of this work demonstrate a striking dissociation between gamma and alpha rhythmic responses in human visual cortex. Gamma oscillations were highly localized and feature-tuned, summating approximately linearly across distinct stimulus subregions, whereas alpha oscillations were broadly distributed, only weakly selective for stimulus features, and showed subadditive suppressive effects consistent with divisive normalization. This dissociation supports the view that gamma and alpha are generated by distinct neural circuits with complementary roles, rather than being merely inverse reflections of a single process.

5.2 Gamma reflects localized excitation and linear field summation

Under the present conditions, gamma-band responses were tightly retinotopic and summed linearly when separate visual patches were stimulated, consistent with primate findings that gamma arises within local cortical networks and reflects the sum of local excitatory drives [14, 28]. Non-overlapping stimuli produced additive gamma responses, implying minimal long-range interaction at the generation stage. Gamma also showed robust feature tuning, including orientation and motion direction, with a reliable bias toward non-cardinal orientations—mirroring the "oblique effect" reported in V1 population activity [7, 13, 15, 16, 31, 54]. This contradicts invasive studies show higher density of cardinal-preferring neurons [16, 31] and perceptual salience of these orientations [7, 16], but inverse-oblique effects have been noted recently in EEG gamma [5] as well as visual perception experiments [54].

The linearity observed in this study matches primate LFP results showing that spatially distant patches generate gamma independently, with saturation only when

local inhibitory feedback engages [14, 28]. Under the conditions employed, non-overlapping cortical regions oscillated autonomously at gamma frequencies, indicating gamma power scaled with summed local activity until interactions or saturation occurred. This supports models in which gamma amplitude reflects local excitatory drive within recurrent E–I loops.

Evidence was also found for a transition from local to global gamma with large, contiguous stimulation. Foveal and full-field conditions produced disproportionately high gamma power, consistent with macaque studies showing small stimuli evoke local gamma, whereas large stimuli synchronize distant sites into a coherent network oscillation with shared orientation preference [28, 36]. Further showed that beyond a critical size, a second, slower gamma component emerges, greatly boosting total gamma power. This secondary peak at 30 Hz was observed in our data only after subtracting out baseline responses, suggesting that lower frequency suppression can 'bleed into' the upper frequencies, masking mid-frequency gamma responses in scalp data. Overall, scalp gamma signals were strongest relative to alpha suppression when large portions of retinotopic cortex oscillated in phase. This suggests EEG/MEG gamma emphasizes the global component of cortical gamma, scaling super-linearly when local generators synchronize. Such network locking explains the reproducibility of gamma frequency and amplitude across cortex and reinforces the view that narrowband gamma indexes coherent cortical excitation, bridging invasive animal studies and human EEG.

5.3 Alpha reflects broad suppression and divisive normalization

Unlike gamma, alpha-band activity showed weak spatial and feature selectivity but was strongly modulated by stimulus presence or expectation. Alpha power dropped sharply whenever a stimulus was anticipated or present, supporting its role as an inverse index of cortical engagement. Enlarging or adding stimuli produced subadditive, saturating suppression: once alpha was already reduced by one patch, a second in a different location caused only a small further drop. This pattern matches divisive normalization models [6, 53], where inhibitory feedback scales down additional responses once a certain drive level is reached. The results of this study suggest alpha indexes this gain-control process, in which overlapping neural populations share an inhibitory signal that limits combined responses. Human ECoG findings similarly show alpha correlating with surround suppression [20], supporting the idea that alpha "tracks" cortical normalization. In effect, gamma summed excitations while alpha divided them, highlighting an antagonistic complementarity. Mechanistically, alpha's lack of strong feature tuning and saturating profile suggests origins in global or downstream networks. Physiological evidence points to generation in higher visual areas and thalamocortical circuits linked to

feedback [4, 52]. In monkey V1, alpha oscillations predominantly arise in layers 5 and 6, propagate in a top-down (feedback) direction from higher-order areas to lower-order visual cortex, and are selectively suppressed when feedback pathways are pharmacologically blocked. In contrast, gamma oscillations persist under these conditions, indicating that alpha reflects feedback-mediated inhibition, while gamma is more tightly linked to local, feedforward processing. Thalamocortical models show a similar 8–12 Hz "idling" state driven by cortex–thalamus–reticular nucleus loops [4], providing rhythmic inhibition until stronger input arrives. Additionally, observations revealed anticipatory alpha suppression, reductions even for 'blank' gray screens following crosshair priming, consistent with top-down modulation. Attention studies that show alpha decreases at attended locations and increases in ignored ones [4, 50], indicating proactive disinhibition to enhance processing. In the 'no-stimulus' cue trials conducted in this study, alpha suppression fit this preparatory role. Overall, alpha's weak feature tuning, broad reach, divisive summation, and context-dependent suppression align with its proposed role as an inhibitory gain-control signal that dynamically regulates cortical excitation.

5.4 Antagonistic but configuration-dependent relationship between gamma and alpha

The investigation examined whether gamma and alpha oscillations always trade off in a simple push–pull fashion or if their relationship depends on stimulus context. In general, an expected inverse coupling was observed: conditions with strong gamma coincided with stronger alpha suppression, consistent with these rhythms jointly maintaining E/I balance [12, 27]. However, the relationship was not uniform across all stimulus manipulations.

During orientation tuning, alpha was strongly suppressed for all gratings relative to blank, with no significant differences between preferred and non-preferred orientations (Though a trend toward stronger suppression for horizontal gratings was observed ($p = 0.15$)). In contrast, gamma power varied sharply with orientation, peaking at oblique angles and showing minima for horizontal orientations. Despite the absence of clear alpha tuning, orientation-averaged alpha and gamma responses were positively correlated across orientations ($r = 0.94$, $p < 0.005$)—a striking reversal of the robust negative gamma–alpha relationship observed for retinotopic manipulations. The stronger alpha suppression for horizontal gratings may reflect anisotropies in early visual cortex, where horizontal orientations—common in natural scenes—drive larger population responses in V1 [7, 16], more effectively disengaging alpha-generating inhibitory networks. In contrast, the global gamma LFP shows reduced responses for horizontals, possibly because gamma in EEG reflects spatial summation of locally coherent oscillations; widespread horizontal activation may recruit more diverse orientation domains with less phase alignment,

lowering the net global gamma amplitude despite strong local spiking activity [28].

Stimulus location and size also shaped the interplay. Foveal and full-field stimuli evoked the strongest gamma responses but relatively weak alpha suppression, whereas peripheral stimulation produced stronger alpha suppression despite weaker gamma. This likely reflects differences in spatial summation: foveal and full field gratings activate a larger, contiguous retinotopic patch, increasing the chance for phase-aligned local generators to sum into strong global gamma, while peripheral stimuli drive more spatially dispersed regions with lower cross-site coherence, limiting global gamma even when alpha suppression is pronounced.

5.5 Implications for oscillation theories and cross-species comparisons

The dissociation in gamma and alpha tuning supports models assigning these rhythms to distinct circuit mechanisms: gamma arising from local recurrent excitatory–inhibitory (E–I) networks under feedforward drive (PING), and alpha from feedback and modulatory circuits imposing inhibitory control [2, 4, 51].

This fits hierarchical frameworks like predictive coding, where alpha/beta carry top-down expectations that suppress predictable inputs and gamma carries bottom-up prediction errors. The finding that alpha can divide down inputs that gamma sums echoes the mechanism of predictive inhibition. It also aligns with "communication through coherence" [12] and "gating by inhibition" [27] models: gamma synchrony aligns high-excitability phases to open communication channels, while alpha increases inhibition to close them. Large, coherent gamma in low-alpha states (as with large stimuli) likely facilitates inter-areal visual communication; high-alpha states (no-stimulus or surround normalization) decouple networks and reduce throughput. Attention exploits this dual mechanism by lowering alpha and boosting gamma in task-relevant regions [33, 50], selectively amplifying some inputs while suppressing others.

The results of this study link human noninvasive measures to invasive animal data. Human EEG gamma shows feature tuning and spatial summation akin to monkey LFP gamma [14, 28, 36], supporting its value for inferring circuit properties, particularly large-scale synchrony. Alpha's broad suppression and context sensitivity match monkey electrophysiology and human MEG [4, 49], reinforcing its role in normalization. Some anisotropies, like the cardinal–oblique bias, are stronger in human population signals than in macaque single units [13, 14, 16, 28, 31, 54]; The gamma results from this study capture this population-level bias, suggesting that gamma is sensitive to ensemble-scale tuning. Alpha's lack of significant orientation bias may reflect greater variability in its pre-stimulus baseline, as suppression depends strongly on the starting level of alpha power rather than on specific stimulus features. Taken together, these findings strengthen a unifying cross-species

view: gamma reflects localized, feature-driven excitation and coherent communication, whereas alpha reflects diffuse, feedback-mediated inhibition and competitive normalization. These complementary rhythms jointly regulate information flow through the visual hierarchy.

5.6 Conclusion

The results of this study reveal a clear dissociation between gamma and alpha rhythms in human visual cortex: gamma was strongly localized, feature-tuned, and summed linearly across non-overlapping regions, whereas alpha was broadly distributed, weakly feature-selective, and showed divisive normalization. Global EEG gamma was maximized when large, contiguous retinotopic regions oscillated coherently (e.g., foveal stimulation), while alpha suppression depended more on pre-stimulus baseline and could be strong even with weak gamma, as in peripheral stimulation. Orientation tuning revealed an unexpected positive alpha–gamma correlation, likely reflecting shared dependence on local excitatory drive, with horizontal gratings producing deeper alpha suppression but weaker global gamma due to reduced cross-site phase alignment. These findings support distinct circuit origins—gamma from local recurrent E–I loops under feedforward drive, alpha from feedback-mediated inhibitory control—and highlight how their interplay depends on stimulus size, location, and feature content. Future experiments could test the mechanisms behind this dissociation by pairing the paradigm with manipulations of attention, expectation, or visual context (e.g., surround suppression) to modulate feedback signals. Applying the same stimuli under varied visual load or task demands, and combining them with source-resolved MEG/EEG or invasive recordings, could more precisely link scalp measures to laminar- and circuit-level generators.

Bibliography

[1] E. D. Adrian and B. H. Matthews, *The berger rhythm: potential changes from the occipital lobes in man*, Brain, 57 (1934), pp. 355–385.

[2] A. M. Bastos, J. Vezoli, C. A. Bosman, J.-M. Schoffelen, R. Oostenveld, J. R. Dowdall, P. De Weerd, H. Kennedy, and P. Fries, *Visual areas exert feedforward and feedback influences through distinct frequency channels*, Neuron, 85 (2015), pp. 390–401.

[3] H. Berger, *Über das elektroenkephalogramm des menschen*, Archiv für psychiatrie und nervenkrankheiten, 87 (1929), pp. 527–570.

[4] A. Bollimunta, J. Mo, C. E. Schroeder, and M. Ding, *Neuronal mechanisms and attentional modulation of corticothalamic alpha oscillations*, Journal of Neuroscience, 31 (2011), pp. 4935–4943.

[5] R. Butler, G. W. Mierzwinski, P.-M. Bernier, M. Descoteaux, G. Gilbert, and K. Whittingstall, *Neurophysiological basis of contrast dependent bold orientation tuning*, NeuroImage, 206 (2020), p. 116323.

[6] M. Carandini and D. J. Heeger, *Normalization as a canonical neural computation*, Nature reviews neuroscience, 13 (2012), pp. 51–62.

[7] E. A. Essock, J. K. DeFord, B. C. Hansen, and M. J. Sinai, *Oblique stimuli are seen best (not worst!) in naturalistic broad-band stimuli: A horizontal effect*, Vision research, 43 (2003), pp. 1329–1335.

[8] C. Fang, X. Cai, and H. D. Lu, *Orientation anisotropies in macaque visual areas*, Proceedings of the National Academy of Sciences, 119 (2022), p. e2113407119.

[9] F. Fang, S. O. Murray, D. Kersten, and S. He, *Orientation-tuned fmri adaptation in human visual cortex*, Journal of neurophysiology, 94 (2005), pp. 4188–4195.

[10] J. J. Foxe and A. C. Snyder, *The role of alpha-band brain oscillations as a sensory suppression mechanism during selective attention*, Frontiers in psychology, 2 (2011), p. 154.

[11] A. Frien, R. Eckhorn, R. Bauer, T. Woelbern, and A. Gabriel, *Fast oscillations display sharper orientation tuning than slower components of the same recordings in striate cortex of the awake monkey*, European Journal of Neuroscience, 12 (2000), pp. 1453–1465.

[12] P. Fries, *Rhythms for cognition: communication through coherence*, Neuron, 88 (2015), pp. 220–235.

[13] C. S. Furmanski and S. A. Engel, *An oblique effect in human primary visual cortex*, Nature neuroscience, 3 (2000), pp. 535–536.

[14] M. Gieselmann and A. Thiele, *Comparison of spatial integration and surround suppression characteristics in spiking activity and the local field potential in macaque v1*, European Journal of Neuroscience, 28 (2008), pp. 447–459.

[15] A. R. Girshick, M. S. Landy, and E. P. Simoncelli, *Cardinal rules: visual orientation perception reflects knowledge of environmental statistics*, Nature neuroscience, 14 (2011), pp. 926–932.

[16] A. Grabska-Barwińska, C. Distler, K.-P. Hoffmann, and D. Jancke, *Contrast independence of cardinal preference: stable oblique effect in orientation maps of ferret visual cortex*, European Journal of Neuroscience, 29 (2009), pp. 1258–1270.

[17] C. M. Gray and W. Singer, *Stimulus-specific neuronal oscillations in orientation columns of cat visual cortex.*, Proceedings of the National Academy of Sciences, 86 (1989), pp. 1698–1702.

[18] A. Hadjipapas, P. Adjamian, J. B. Swettenham, I. E. Holliday, and G. R. Barnes, *Stimuli of varying spatial scale induce gamma activity with distinct temporal characteristics in human visual cortex*, Neuroimage, 35 (2007), pp. 518–530.

[19] T. Hakami, N. C. Jones, E. A. Tolmacheva, J. Gaudias, J. Chaumont, M. Salzberg, T. J. O'Brien, and D. Pinault, *Nmda receptor hypofunction leads to generalized and persistent aberrant γ oscillations independent of hyperlocomotion and the state of consciousness*, PloS one, 4 (2009), p. e6755.

[20] B. M. Harvey, M. J. Vansteensel, C. H. Ferrier, N. Petridou, W. Zuiderbaan, E. J. Aarnoutse, M. G. Bleichner, H. C. Dijkerman, M. J. van Zandvoort, F. S. Leijten, et al., *Frequency specific spatial interactions in human electrocorticography: V1 alpha oscillations reflect surround suppression*, Neuroimage, 65 (2013), pp. 424–432.

[21] D. Hermes, K. Miller, B. Wandell, and J. Winawer, *Stimulus dependence of gamma oscillations in human visual cortex*, Cerebral cortex, 25 (2015), pp. 2951–2959.

[22] S. W. Hong, *Radial bias for orientation and direction of motion modulates access to visual awareness during continuous flash suppression*, Journal of Vision, 15 (2015), pp. 3–3.

[23] D. H. Hubel and T. N. Wiesel, *Receptive fields, binocular interaction and functional architecture in the cat's visual cortex*, The Journal of physiology, 160 (1962), p. 106.

[24] A. M. Ichim, H. Barzan, V. V. Moca, A. Nagy-Dabacan, A. Ciuparu, A. Hapca, K. Vervaeke, and R. C. Muresan, *The gamma rhythm as a guardian of brain health*, eLife, 13 (2024), p. e100238.

[25] J. Iivanainen, R. Zetter, and L. Parkkonen, *Potential of on-scalp meg: Robust detection of human visual gamma-band responses*, Human brain mapping, 41 (2020), pp. 150–161.

[26] C.-H. Im, A. Gururajan, N. Zhang, W. Chen, and B. He, *Spatial resolution of eeg cortical source imaging revealed by localization of retinotopic organization in human primary visual cortex*, Journal of neuroscience methods, 161 (2007), pp. 142–154.

[27] O. Jensen and A. Mazaheri, *Shaping functional architecture by oscillatory alpha activity: gating by inhibition*, Frontiers in human neuroscience, 4 (2010), p. 186.

[28] X. Jia, M. A. Smith, and A. Kohn, *Stimulus selectivity and spatial coherence of gamma components of the local field potential*, Journal of Neuroscience, 31 (2011), pp. 9390–9403.

[29] X. Jia, S. Tanabe, and A. Kohn, *Gamma and the coordination of spiking activity in early visual cortex*, Neuron, 77 (2013), pp. 762–774.

[30] S. P. Kelly, E. C. Lalor, R. B. Reilly, and J. J. Foxe, *Increases in alpha oscillatory power reflect an active retinotopic mechanism for distracter suppression during sustained visuospatial attention*, Journal of neurophysiology, 95 (2006), pp. 3844–3851.

[31] B. Li, M. R. Peterson, and R. D. Freeman, *Oblique effect: a neural basis in the visual cortex*, Journal of neurophysiology, 90 (2003), pp. 204–217.

[32] Y. Li, W. Bosking, M. S. Beauchamp, S. A. Sheth, D. Yoshor, E. Bartoli, and B. L. Foster, *Biased orientation and color tuning of the human visual gamma rhythm*, Journal of Neuroscience, 42 (2022), pp. 1054–1067.

[33] K. E. Mathewson, A. Lleras, D. M. Beck, M. Fabiani, T. Ro, and G. Gratton, *Pulsed out of awareness: Eeg alpha oscillations represent a pulsed-inhibition of ongoing cortical processing*, Frontiers in psychology, 2 (2011), p. 99.

[34] A. Mazaheri and O. Jensen, *Rhythmic pulsing: Linking ongoing brain activity withrhythmic pulsing: Linking ongoing brain activity with evoked responses*, Frontiers in Human Neuroscience, 4 (2010).

[35] G. Michalareas, J. Vezoli, S. Van Pelt, J.-M. Schoffelen, H. Kennedy, and P. Fries, *Alpha-beta and gamma rhythms subserve feedback and feedforward influences among human visual cortical areas*, Neuron, 89 (2016), pp. 384–397.

[36] D. V. Murty, V. Shirhatti, P. Ravishankar, and S. Ray, *Large visual stimuli induce two distinct gamma oscillations in primate visual cortex*, Journal of Neuroscience, 38 (2018), pp. 2730–2744.

[37] S. D. Muthukumaraswamy and K. D. Singh, *Visual gamma oscillations: the effects of stimulus type, visual field coverage and stimulus motion on meg and eeg recordings*, Neuroimage, 69 (2013), pp. 223–230.

[38] E. V. Orekhova, A. V. Butorina, O. V. Sysoeva, A. O. Prokofyev, A. Y. Nikolaeva, and T. A. Stroganova, *Frequency of gamma oscillations in humans is modulated by velocity of visual motion*, Journal of neurophysiology, 114 (2015), pp. 244–255.

[39] G. Perry, K. Hamandi, L. M. Brindley, S. D. Muthukumaraswamy, and K. D. Singh, *The properties of induced gamma oscillations in human visual cortex show individual variability in their dependence on stimulus size*, Neuroimage, 68 (2013), pp. 83–92.

[40] D. Pinault, *N-methyl d-aspartate receptor antagonists ketamine and mk-801 induce wake-related aberrant γ oscillations in the rat neocortex*, Biological psychiatry, 63 (2008), pp. 730–735.

[41] T. A. Rihs, C. M. Michel, and G. Thut, *Mechanisms of selective inhibition in visual spatial attention are indexed by α-band eeg synchronization*, European Journal of Neuroscience, 25 (2007), pp. 603–610.

[42] Y. Sasaki, R. Rajimehr, B. W. Kim, L. B. Ekstrom, W. Vanduffel, and R. B. Tootell, *The radial bias: a different slant on visual orientation sensitivity in human and nonhuman primates*, Neuron, 51 (2006), pp. 661–670.

[43] R. Scheeringa, P. J. Koopmans, T. van Mourik, O. Jensen, and D. G. Norris, *The relationship between oscillatory eeg activity and the laminar-specific bold signal*, Proceedings of the National Academy of Sciences, 113 (2016), pp. 6761–6766.

[44] D. S. Schwarzkopf, D. J. Robertson, C. Song, G. R. Barnes, and G. Rees, *The frequency of visually induced gamma-band oscillations depends on the size of early human visual cortex*, Journal of Neuroscience, 32 (2012), pp. 1507–1512.

[45] M. I. Sereno, A. M. Dale, J. B. Reppas, K. K. Kwong, J. W. Belliveau, T. J. Brady, B. R. Rosen, and R. B. Tootell, *Borders of multiple visual areas in humans revealed by functional magnetic resonance imaging*, Science, 268 (1995), pp. 889–893.

[46] B. J. Stauch, A. Peter, I. Ehrlich, Z. Nolte, and P. Fries, *Human visual gamma for color stimuli*, Elife, 11 (2022), p. e75897.

[47] J. B. Swettenham, S. D. Muthukumaraswamy, and K. D. Singh, *Spectral properties of induced and evoked gamma oscillations in human early visual cortex to moving and stationary stimuli*, Journal of neurophysiology, 102 (2009), pp. 1241–1253.

[48] C. Tallon-Baudry and O. Bertrand, *Oscillatory gamma activity in humans and its role in object representation*, Trends in cognitive sciences, 3 (1999), pp. 151–162.

[49] L. Tarhan and T. Konkle, *Reliability-based voxel selection*, NeuroImage, 207 (2020), p. 116350.

[50] G. Thut, A. Nietzel, S. A. Brandt, and A. Pascual-Leone, *α-band electroencephalographic activity over occipital cortex indexes visuospatial attention bias and predicts visual target detection*, Journal of neuroscience, 26 (2006), pp. 9494–9502.

[51] T. Van Kerkoerle, M. W. Self, B. Dagnino, M.-A. Gariel-Mathis, J. Poort, C. Van Der Togt, and P. R. Roelfsema, *Alpha and gamma oscillations characterize feedback and feedforward processing in monkey visual cortex*, Proceedings of the National Academy of Sciences, 111 (2014), pp. 14332–14341.

[52] T. Van Kerkoerle, M. W. Self, and P. R. Roelfsema, *Layer-specificity in the effects of attention and working memory on activity in primary visual cortex*, Nature communications, 8 (2017), p. 13804.

[53] M. J. Wainwright and O. Schwartz, *10 natural image statistics and divisive*, Probabilistic models of the brain: Perception and neural function, 203 (2002).

[54] H. R. Wilson, G. Loffler, F. Wilkinson, and W. A. Thistlethwaite, *An inverse oblique effect in human vision*, Vision Research, 41 (2001), pp. 1749–1753.

[55] T. Womelsdorf, P. Fries, P. P. Mitra, and R. Desimone, *Gamma-band synchronization in visual cortex predicts speed of change detection*, Nature, 439 (2006), pp. 733–736.

[56] M. S. Worden, J. J. Foxe, N. Wang, and G. V. Simpson, *Anticipatory biasing of visuospatial attention indexed by retinotopically specific alpha-band electroencephalography increases over occipital cortex.*, The Journal of neuroscience: the official journal of the Society for Neuroscience, 20 (2000), pp. RC63–RC63.